AGU PUBLICATIONS

Global Biogeochemical Cycles

RESEARCH ARTICLE

10.1002/2014GB004890

Key Points:

- Accurate attribution of CO_2 variability is required to constrain coupled models
- Combined influence of drought and fire exceed ecosystem responses to temperature
- Temporal and spatial smoothing of CO_2 observations masks variability from fire

Correspondence to:
G. Keppel-Aleks,
gkeppela@umich.edu

Citation:
Keppel-Aleks, G., A. S. Wolf, M. Mu, S. C. Doney, D. C. Morton, P. S. Kasibhatla, J. B. Miller, E. J. Dlugokencky, and J. T. Randerson (2014), Separating the influence of temperature, drought, and fire on interannual variability in atmospheric CO_2, *Global Biogeochem. Cycles*, *28*, 1295–1310, doi:10.1002/2014GB004890.

Received 6 MAY 2014
Accepted 3 OCT 2014
Accepted article online 7 OCT 2014
Published online 19 NOV 2014

Separating the influence of temperature, drought, and fire on interannual variability in atmospheric CO_2

Gretchen Keppel-Aleks[1], Aaron S. Wolf[2], Mingquan Mu[3], Scott C. Doney[4], Douglas C. Morton[5], Prasad S. Kasibhatla[6], John B. Miller[7,8], Edward J. Dlugokencky[8], and James T. Randerson[3]

[1]Department of Atmospheric, Oceanic, and Space Sciences, University of Michigan, Ann Arbor, Michigan, USA, [2]Department of Earth and Environmental Science, University of Michigan, Ann Arbor, Michigan, USA, [3]Department of Earth System Science, University of California, Irvine, California, USA, [4]Department of Marine Chemistry and Geochemistry, Woods Hole Oceanographic Institution, Woods Hole, Massachusetts, USA, [5]Biospheric Sciences Laboratory, NASA Goddard Space Flight Center, Greenbelt, Maryland, USA, [6]Nicholas School of the Environment, Duke University, Durham, North Carolina, USA, [7]Cooperative Institute for Research in Environmental Sciences, University of Colorado Boulder, Boulder, Colorado, USA, [8]NOAA Earth System Research Laboratory, Global Monitoring Division, Boulder, Colorado, USA

Abstract The response of the carbon cycle in prognostic Earth system models (ESMs) contributes significant uncertainty to projections of global climate change. Quantifying contributions of known drivers of interannual variability in the growth rate of atmospheric carbon dioxide (CO_2) is important for improving the representation of terrestrial ecosystem processes in these ESMs. Several recent studies have identified the temperature dependence of tropical net ecosystem exchange (NEE) as a primary driver of this variability by analyzing a single, globally averaged time series of CO_2 anomalies. Here we examined how the temporal evolution of CO_2 in different latitude bands may be used to separate contributions from temperature stress, drought stress, and fire emissions to CO_2 variability. We developed atmospheric CO_2 patterns from each of these mechanisms during 1997–2011 using an atmospheric transport model. NEE responses to temperature, NEE responses to drought, and fire emissions all contributed significantly to CO_2 variability in each latitude band, suggesting that no single mechanism was the dominant driver. We found that the sum of drought and fire contributions to CO_2 variability exceeded direct NEE responses to temperature in both the Northern and Southern Hemispheres. Additional sensitivity tests revealed that these contributions are masked by temporal and spatial smoothing of CO_2 observations. Accounting for fires, the sensitivity of tropical NEE to temperature stress decreased by 25% to 2.9 ± 0.4 Pg C yr^{-1} K^{-1}. These results underscore the need for accurate attribution of the drivers of CO_2 variability prior to using contemporary observations to constrain long-term ESM responses.

1. Introduction

Observed variations in the growth rate of atmospheric carbon dioxide, CO_2, provide insight about the processes that govern land and ocean sinks for anthropogenic CO_2. Interannual variability in atmospheric CO_2 is tightly linked with volcanic eruptions [*Farquhar and Roderick*, 2003; *Frölicher et al.*, 2013] and climate modes, including El Niño–Southern Oscillation (ENSO) [*Bacastow*, 1976; *Jones et al.*, 2001; *Zeng et al.*, 2005; *Schwalm et al.*, 2011]. Evidence from carbon isotopes suggests that these CO_2 variations originate mostly from terrestrial ecosystems, rather than ocean carbon exchange [*Francey et al.*, 1995; *Battle et al.*, 2000; *Rayner et al.*, 2008; *Alden et al.*, 2010].

Recent work has improved our understanding of the underlying processes regulating variability in carbon fluxes within terrestrial ecosystems. Many studies have noted a positive correlation between land temperature anomalies and the atmospheric CO_2 growth rate [*Keeling et al.*, 1995; *Braswell*, 1997; *Rafelski et al.*, 2009], especially during the warm El Niño phase of ENSO [*Wang et al.*, 2013]. Tropical ecosystem responses to warmer temperature tend to release CO_2 to the atmosphere as a consequence of several physiological processes that operate in concert. Specifically, gross primary production (GPP) in tropical forests generally decreases in response to lower carboxylation efficiency and other stresses [*Berry and Bjorkman*, 1980; *Doughty and Goulden*, 2008]. Autotrophic respiration responses also likely contribute to carbon losses as a consequence of greater leaf, stem, and root maintenance costs. In parallel, microbial responses to higher temperature cause

decomposition to accelerate [*Atkin*, 2003; *Davidson and Janssens*, 2006; *Mahecha et al.*, 2010], increasing emissions from litter and soil organic matter. These plant and microbial responses to temperature are widely represented in terrestrial ecosystem models, albeit with varying temperature dependencies [*Todd-Brown et al.*, 2013]. We hereafter refer to the combined set of these canopy-scale processes (and their temperature dependencies) as the direct temperature response of net ecosystem exchange (NEE); alone, this response is sufficient to generate a strong positive relationship between interannual temperature variations and tropical CO_2 fluxes in models [*Wang et al.*, 2013].

Climate modes also modify hydrology, complicating explanations of atmospheric CO_2 variability that rely solely on NEE responses to temperature. Shifts in atmospheric circulation from Pacific or Atlantic sea surface temperature anomalies modify rainfall in tropical and subtropical terrestrial ecosystems [*Ropelewski and Halpert*, 1987; *Nobre and Shukla*, 1996]. In certain wet tropical forests, seasonal or interannual drought reduces soil respiration considerably, whereas GPP may be less affected as a consequence of increased light availability and the ability of deeply rooted trees to withstand desiccation of surface soil layers [*Saleska et al.*, 2003; *Bonal et al.*, 2008]. Due to a paucity of data, it remains unclear how tropical drought responses vary along moisture gradients or with vegetation type; however, top-down constraints from atmospheric CO_2 suggest that in the Amazon, basin-wide net carbon uptake is reduced in drought years [*Gatti et al.*, 2014]. In temperate ecosystems, eddy covariance observations likewise indicate that, overall, drought-induced reductions in GPP exceed those for ecosystem respiration, and therefore, net carbon uptake is reduced [*Schwalm et al.*, 2010].

In addition to the temperature and drought stress impacts on NEE described above, fires also contribute to atmospheric CO_2 variability on interannual time scales. Fire emissions are usually confined to the dry season in tropical forests and are regulated both by climate and human drivers [*van der Werf et al.*, 2010; *Bowman et al.*, 2011]. In savannas, drought conditions often increase burning in woodlands but reduce fuel availability and emissions in drier grasslands [*Randerson et al.*, 2005]. Fires also contribute to interannual variability in atmospheric methane (CH_4) [*Bousquet et al.*, 2006] and are a dominant driver of interannual variability in carbon monoxide (CO) [*Langenfelds et al.*, 2002; *van der Werf et al.*, 2004]. When CH_4 and CO observations are combined with measurements of emission ratios from smoke plumes [*Andreae and Merlet*, 2001; *Akagi et al.*, 2011], they provide evidence for a significant contribution from fires to variability in atmospheric CO_2 [*Langenfelds et al.*, 2002; *van der Werf et al.*, 2004; *Gatti et al.*, 2014].

Partitioning the observed variability in atmospheric CO_2 to temperature, drought, and fire drivers remains an important research challenge because the correct balance of mechanisms is needed to simulate the global carbon cycle accurately in Earth system models (ESMs). Recently, *Wang et al.* [2013] found that the temperature sensitivity of tropical NEE was the dominant mechanism explaining CO_2 interannual variability, with considerably weaker controls from precipitation-induced changes in NEE and even smaller contributions from fires. Similarly, *Cox et al.* [2013] found that heterotrophic respiration responses in C4MIP models were the primary drivers of model-to-model differences in the sensitivity of tropical NEE to temperature, with no explicit estimate of fire emissions considered in model comparisons with observations. In both studies, the CO_2 record used in the analysis was a globally averaged time series that was further temporally smoothed during estimation of the growth rate, either by using a 12 month running mean [*Wang et al.*, 2013] or by differencing the annual means from two consecutive years [*Cox et al.*, 2013].

Here we examined how higher-resolution atmospheric CO_2 data may improve the attribution process. An important motivation was the observation that many of the climate extremes over the last several decades have been confined to specific regions [*Reichstein et al.*, 2013], and thus, biospheric responses to these events likely leave an asymmetric (and unique) imprint on the meridional distribution of CO_2. In addition, emission anomalies from fires are phase locked to the dry season in tropical forests and are closely associated with regional hotspots of land use change, further enabling separation of this tracer from NEE responses to temperature and drought stress.

In section 2, we describe our method to simulate interannual variability in atmospheric CO_2 from simple basis fluxes derived from gridded climate data. These basis fluxes were propagated through an atmospheric transport model [*Suntharalingam et al.*, 2004; *Nassar et al.*, 2010], enabling direct comparison of simulated CO_2 against meridional and temporal patterns in monthly atmospheric observations. In section 3, we present the relative contribution of individual drivers and combinations thereof to the observed interannual

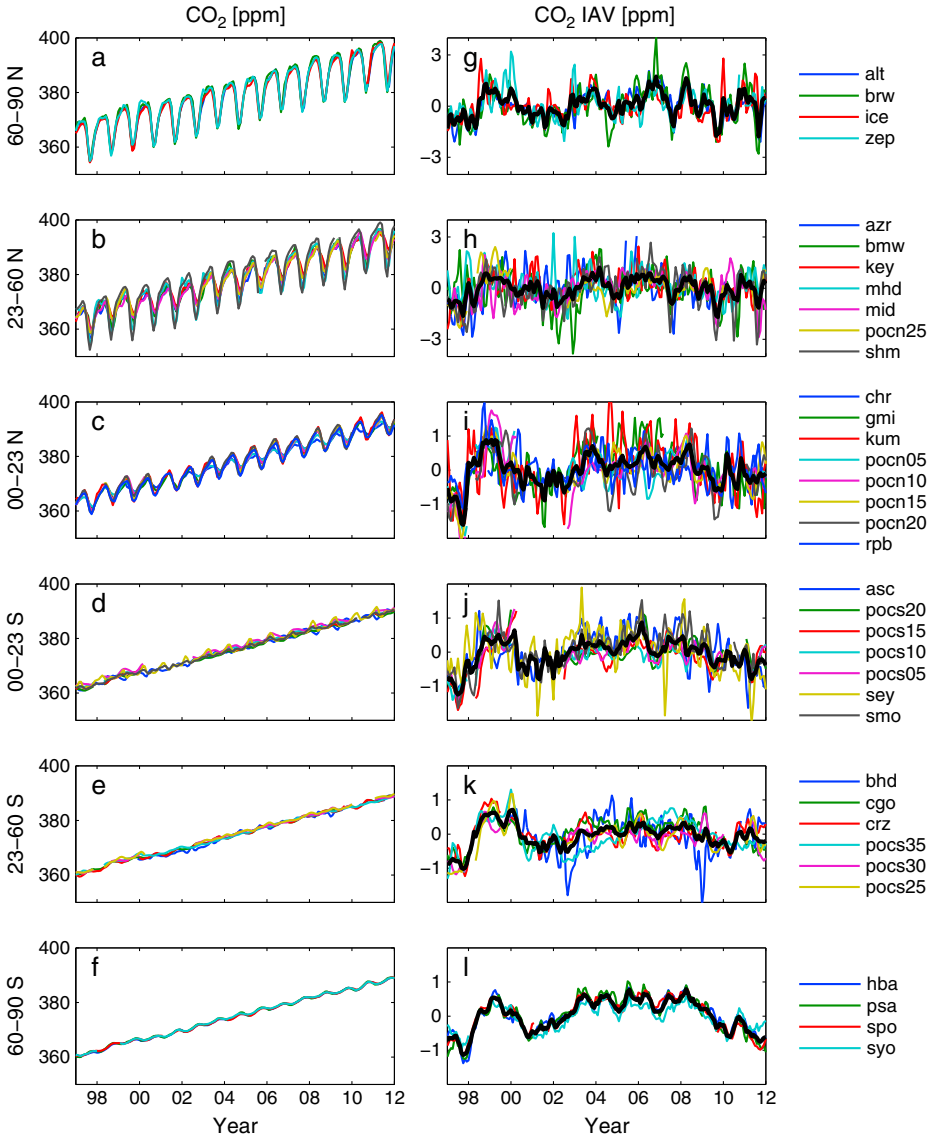

Figure 1. Observations of atmospheric CO_2 from 1997 to 2011 in different latitude bands. (a–f) Original monthly mean time series and (g–l) the interannual component of atmospheric CO_2 variations from marine boundary layer (MBL) sites in the NOAA ESRL global cooperative air sampling network. Observations were binned into six latitude bands for comparison with simulated CO_2. Station acronyms and location information appear in Table 1.

variability of CO_2 during 1997–2011 determined from optimal estimation. In section 4, we discuss how the interplay among these drivers provides both improved estimates of the climate sensitivity of NEE and directions for reducing carbon cycle uncertainties in ESMs.

2. Data and Methods

2.1. Atmospheric CO_2 Observations

We analyzed CO_2 interannual variability for the 15 year period from 1997 through 2011 using monthly mean NOAA global cooperative air sampling network observations [*Dlugokencky et al.*, 2013] at marine boundary layer (MBL) sites with greater than 70% data coverage for the time period of interest (Figures 1a–1f and Table 1). We chose this period based on the availability of fire emissions data [*van der Werf et al.*, 2010] to compare with temperature and drought effects. CO_2 interannual variability was calculated by (1) detrending

Table 1. Marine Boundary Layer (MBL) Sites in NOAA's Global Cooperative Air Sampling Network

Region	Station	Acronym	Latitude [°N]	Longitude [°E]
60–90°N	Alert, Nunavut, Canada	ALT	82.5	−62.5
	Ny Ålesund, Svalbard	ZEP	78.9	11.9
	Barrow, Alaska	BRW	71.3	−156.6
	Storhofdi, Iceland	ICE	63.4	−20.1
23–60°N	Mace Head, Ireland	MHD	53.3	−9.9
	Shemya, Alaska	SHM	52.7	174.1
	Terceira Island, Azores	AZR	38.8	−27.4
	Tudor Hill, Bermuda	BMW	32.3	−64.7
	Midway Island	MID	28.2	−177.4
	Key Biscayne, Florida	KEY	25.7	−80.2
	Pacific Ocean 25°N	POCN25	25.0	−139.0
0–23°N	Pacific Ocean 20°N	POCN20	20.0	−141.0
	Cape Kumukahi, Hawaii	KUM	19.5	225.0
	Pacific Ocean 15°N	POCN15	15.0	−145.0
	Mariana Islands, Guam	GMI	13.4	144.8
	Ragged Point, Barbados	RPB	13.2	−59.4
	Pacific Ocean 10°N	POCN10	10.0	−149.0
	Pacific Ocean 5°N	POCN05	5.0	−151.0
0–23°S	Mahe Island, Seychelles	SEY	−4.7	55.2
	Pacific Ocean 5°S	POCS05	−5.0	−159.0
	Ascension Island	ASC	−8.0	−14.4
	Pacific Ocean 10°S	POCS10	−10.0	−161.0
	Tutuila, American Samoa	SMO	−14.3	−170.6
	Pacific Ocean 15°S	POCS15	−15.0	−171.0
	Pacific Ocean 20°S	POCS20	−20.0	−174.0
23–60°S	Pacific Ocean 25°S	POCS25	−25.0	−171.0
	Pacific Ocean 30°S	POCS30	−30.0	−176.0
	Pacific Ocean 35°S	POCS35	−35.0	−180.0
	Cape Grim, Tasmania	CGO	−40.7	144.7
	Baring Head, New Zealand	BHD	−41.0	174.0
	Crozet Island	CRZ	−46.5	51.9
60–90°S	Palmer Station, Antarctica	PSA	−64.0	−64.0
	Syowa, Antarctica	SYO	−69.0	39.6
	Halley Bay, Antarctica	HBA	−75.6	−26.5
	South Pole	SPO	−90.0	−24.8

the observed time series at each site with a third-order polynomial, (2) computing a mean annual cycle from the detrended time series, (3) removing the mean annual cycle from the original time series, and (4) fitting a third-order polynomial to the time series obtained from step (3) [*Keppel-Aleks et al.*, 2013]. Our results were largely insensitive to the method of calculating the monthly mean CO_2 or to detrending methodology (data not shown). We averaged the CO_2 time series into six bands encompassing the tropics, midlatitude, and high latitude in each hemisphere for comparison with simulated CO_2 response functions (Figures 1g–1l). Although the resulting time series for CO_2 variability share similarities, each band is influenced by a different mix of local and remote fluxes modified by atmospheric transport.

2.2. Atmospheric CO_2 Simulated From Simple Basis Fluxes

We simulated monthly mean CO_2 patterns arising from prescribed fluxes using the GEOS-Chem atmospheric transport model, version 9.1.2 [*Suntharalingam et al.*, 2004; *Nassar et al.*, 2010]. The model was driven by 3- to 6-hourly Modern Era Retrospective-Analysis for Research and Applications reanalysis meteorology [*Rienecker et al.*, 2011] at 4° (latitude) by 5° (longitude) horizontal resolution with 47 vertical layers. We sampled monthly mean model output at the grid cells containing the MBL sites, and we detrended and binned simulated CO_2 identically to the observations. CO_2 response functions from individual basis fluxes were carried as individual tracers.

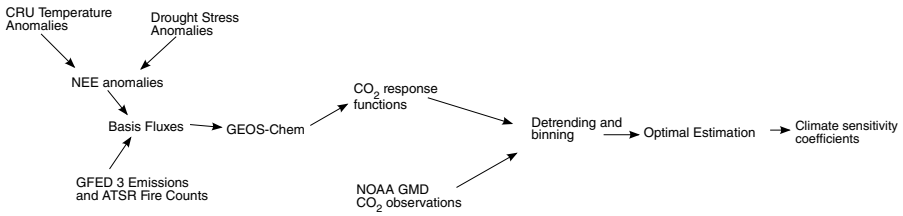

Figure 2. Flow chart for optimal estimation of model parameters and climate sensitivity coefficients.

We used spatially resolved monthly climate time series to construct a series of NEE sensitivity basis fluxes without closely tying our results to the parameterizations of any specific ecosystem model (Figure 2). These fluxes were uniform across an entire month. To represent the influence of temperature stress on NEE, we used land air temperature anomalies at 5° by 5° resolution from the Climatic Research Unit (CRU) at the Hadley Centre [*Jones et al.*, 2012]. We modeled the interannually varying component of the NEE flux due to temperature variations (NEE_T) as follows:

$$NEE_T(t,x,y) = \kappa_T \times \left(T(t,x,y) - \overline{T(m,x,y)}\right) \times Q_{10}^{\left(\frac{\overline{T(m,x,y)}-20}{10}\right)} \times NPP(x,y) \quad (1)$$

where the temperature anomaly at each grid cell from its monthly long-term mean ($T(t,x,y) - \overline{T(m,x,y)}$) is scaled by the annually integrated net primary production (NPP), following the assumption that the magnitude of monthly NEE anomalies at a particular location should be proportional to gross ecosystem fluxes at the same location. In equation (1), t represents time (year and month), while m represents month of the year for the long-term temperature climatology, x represents latitude, and y represents longitude. For the gridded annual mean NPP fluxes we used a climatological estimate derived from the Carnegie-Ames-Stanford Approach (CASA) biogeochemical model at a 1° by 1° resolution [*Randerson et al.*, 1997]. Given the high degree of spatial correlation of annual NPP from models derived from satellite estimates of the fraction of absorbed photosynthetically active radiation and that we only used NPP to scale the spatial pattern of time-evolving NEE anomalies, the results we present have only a marginal sensitivity to specific parameterizations within the biogeochemical model. We included an exponential term ($Q_{10} = 2$) that reduced the impact of temperature anomalies at colder temperatures. The normalization constant κ_T was determined such that the standard deviation in annually integrated NEE_T was 1 Pg C yr^{-1} globally over 15 years.

This model assumes that NEE variations on interannual time scales can be represented as a linear perturbation of temperature anomalies, with the magnitude of the response proportional to the gross ecosystem fluxes in a given region. Although ecosystems may exhibit nonlinear or threshold responses to temperature or drought stress [*Berry and Bjorkman*, 1980; *Reichstein et al.*, 2013], we caution that discriminating and fitting such nonlinear responses within the 15 year duration of our study period would lead to a loss in the robustness of our results given the required increase in the number of fitting parameters and degrees of freedom. Analysis of nonlinear climate impacts on terrestrial ecosystem fluxes may better be suited for future analysis when longer global time series of fire emissions and ecosystem fluxes permit the use of more sophisticated statistical models.

Similarly, we developed a family of basis fluxes to represent the impact of drought stress (D) on NEE (NEE_D) using three drivers that reflect moisture stress on different time scales. We used precipitation from the Global Precipitation Climatology Project (GPCP) [*Adler et al.*, 2003], which reflects the short-term water inputs to the ecosystem. We also used two metrics from NCEP reanalysis climatology [*Kalnay et al.*, 1996]: Palmer Drought Severity Index (PDSI) [*Dai et al.*, 2004], which reflects the cumulative departure from local moisture balance, and potential evaporation (PE), which reflects the evaporative demand given a sufficient soil water source. We used a similar framework to estimate the perturbation to NEE (NEE_D) from drought stress (D) for each of these proxies:

$$NEE_D(t,x,y) = \kappa_D \times (D(t,x,y) - \overline{D(m,x,y)}) \times NPP(x,y) \quad (2)$$

As in equation (1), κ_D was a normalization constant such that each gridded NEE_D time series had a global standard deviation of 1 Pg C yr^{-1} from 1997 to 2011. For this convention, CO_2 fluxes were positive to the atmosphere when precipitation had a positive deviation relative to climatology and when PDSI was in a positive phase (indicating water abundance).

For fires, we used emissions from the Global Fire Emissions Database (GFED3) [*van der Werf et al.*, 2010], which combines satellite observations of active fire counts, burned area, and vegetation productivity with the CASA biogeochemical model to calculate fire emissions. We also prescribed a mostly independent set of fire emissions scaled according to the Along-Track Scanning Radiometer (ATSR) distribution of active fires [*Arino and Melinotte*, 1998]. Because ATSR is a polar-orbiting satellite and therefore oversamples fires at high latitudes relative to midlatitude and tropical fires, we scaled the ATSR fire counts in 10° latitude bins by the fraction of GFED emissions occurring within each bin, thus imposing GFED's latitudinal emissions distribution while preserving distinct patterns of variability between the two basis flux sets.

2.3. Optimal Estimation

Simulated CO_2 response functions from global and regional fluxes were compared against observed interannual variability either individually or in linear combination. We determined scale factors, λ, for each driver included in the model by minimizing the cost function:

$$L = \sum_{\varphi=1}^{6} \left(0.5 \sum_{t=1}^{N} \left(\frac{CO_2(\varphi,t) - \boldsymbol{\lambda} \cdot \mathbf{M}(\varphi,t)}{\sigma(\varphi)} \right)^2 + N \ln \sigma(\varphi) \right) \quad (3)$$

In equation (3), CO_2 (φ,t) is the observed interannual variability in each latitude band, φ. The matrix $\mathbf{M}(\varphi,t)$ contains the individual CO_2 response functions simulated by GEOS-Chem from driver fluxes with 1 Pg C yr^{-1} standard deviation. The vector $\boldsymbol{\lambda}$ contains the optimal scale factors that modulate the standard deviation of the fluxes in each model case. We did not expect that our simple flux models would account for all variability across each latitude band. In the Northern Hemisphere, for instance, observations were characterized by greater temporal variability that likely owes to contributions from fossil fuel fluxes and other processes that were not resolved in our modeling framework. We therefore simultaneously fit parameters $\sigma(\varphi)$ to represent the unresolved variability in each latitude band. Their optimal values reflect the balance between the sum-squared residual and penalty terms of the cost function that resulted in each latitude band contributing equally to the overall sum-squared residual. Our optimizations were conducted without prior constraints on the fluxes. To account for correlations among successive months, we determined the effective number of CO_2 observations in each latitude band assuming an autoregressive (AR1) model and inflated the posterior error covariance matrix by the ratio of actual to effective sample size. We tested the sensitivity of the results to different cost function formulations by weighting the six latitude bands by area fraction and by assuming a *t* distribution for errors. In each case, the optimized λ values remained within the reported error bars, demonstrating the robustness of the optimization results presented in section 3.

We assessed the quality of our regression models for each latitude band using both the familiar Pearson's R^2 coefficient (which indicates the degree of correspondence between model and data) and the RMS amplitude factor. The amplitude factor, *A*, was calculated as a ratio of the standard deviation in the simulated CO_2 time series (adjusted by the appropriate λ values) to the standard deviation in the observed CO_2 time series (equation (4)) and therefore provides information about the magnitude of variability explained by each flux model.

$$A(\varphi) = \frac{\mathrm{std}(\boldsymbol{\lambda}\mathbf{M}(\varphi))}{\mathrm{std}(CO_2(\varphi))} \quad (4)$$

We used the *F* test to compare the relative performance of different regression models; for this test, the number of data was adjusted by the effective sampling rate calculated from the AR1 model. We also used posterior predictive model checking [*Gelman et al.*, 1996] to test whether synthetic CO_2 data generated from our optimized regression models reproduced the observed correlations among temperature, drought, and fire. This provides a quality metric that focuses specifically on the ability to faithfully attribute signal

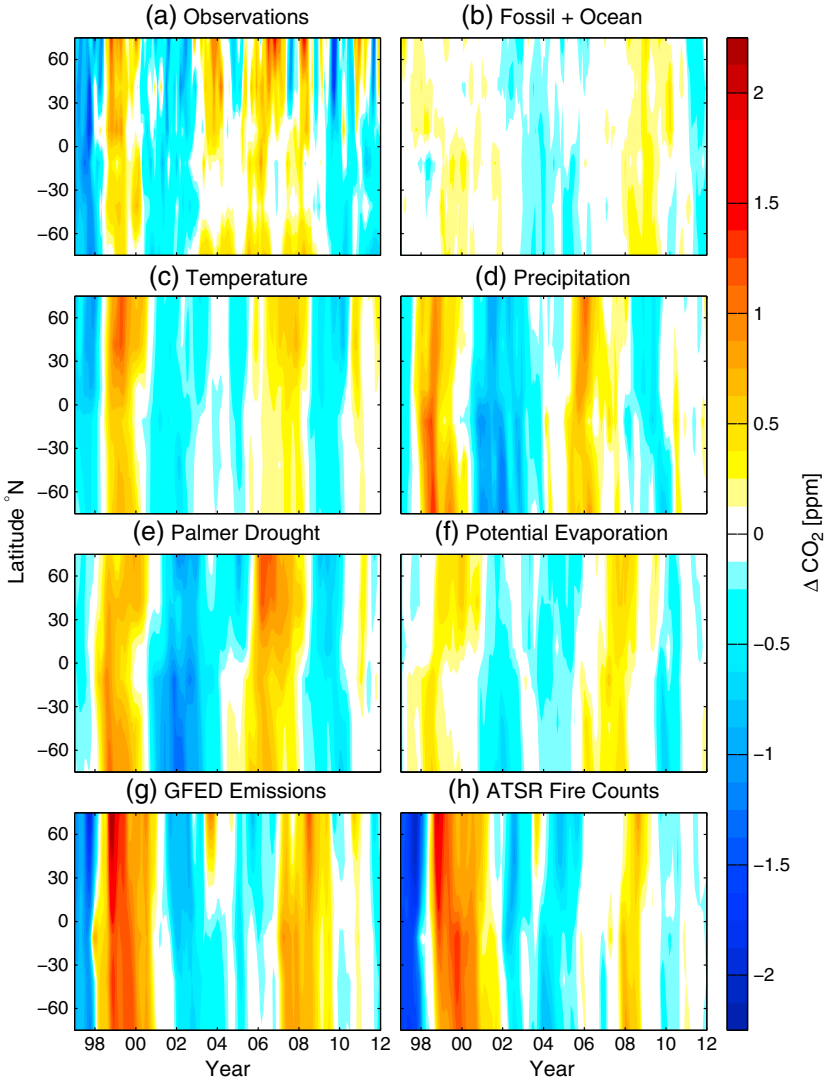

Figure 3. Hovmöller diagrams for observed and simulated CO_2 interannual variability. (a) Observed variability determined from MBL sites (Figure 1 and Table 1). (b) CO_2 response functions derived from the sum of fossil fuel and ocean fluxes. (c) CO_2 response function derived from the temperature sensitivity of NEE. CO_2 response functions derived from the drought sensitivity of NEE determined from (d) precipitation, (e) Palmer Drought Severity Index (PDSI), and (f) potential evaporation (PE). The CO_2 patterns arising from drought stress metrics were scaled by -1, since the simulated patterns were negatively correlated with the observations. CO_2 response functions from fire emissions from (g) the Global Fire Emissions Database version 3 (GFED3) and (h) scaled Along Track Scanning Radiometer (ATSR) fire counts. *X* axis tick marks and year labels correspond to the beginning of each calendar year.

to each driver, rather than just reflecting the overall goodness of fit as given by the R^2 coefficient. This model comparison was carried out by fitting synthetic data using single-driver, single-region regression models and by comparing the resulting λ values to those determined from fits to the observations themselves.

3. Results

CO_2 fluxes from temperature, drought, and fire emissions captured many of the large-scale features in observed atmospheric CO_2 variability from 1997 to 2011 (Figure 3). Contributions from fossil [*Andres et al.*, 2011] and ocean fluxes [*Doney et al.*, 2009] (Figure 3b) were relatively small across all latitudes and consistent with earlier work [*Bousquet et al.*, 2000; *Nevison et al.*, 2008; *Rayner et al.*, 2008]. We optimized scale factors (λ) for each of the terrestrial CO_2 response functions using single-factor regression models

Table 2. The Contribution of Terrestrial Ecosystem Fluxes to Interannual Variability in Atmospheric CO_2 From Single-Variable Global Flux Models[a]

	Global		60–90°N		23–60°N		0–23°N		0–23°S		23–60°S		60–90°S		
	R^2	A	R^2	A	R^2	A	R^2	A	R^2	A	R^2	A	R^2	A	λ
Temperature	0.46	0.61	0.33	0.57	0.25	0.67	0.47	0.65	0.50	0.58	0.60	0.66	0.63	0.52	0.80 ± 0.07
PDSI	0.42	0.55	0.24	0.40	0.31	0.44	0.39	0.49	0.41	0.63	0.66	0.73	0.48	0.60	-0.47 ± 0.05
GFED3	0.36	0.51	0.24	0.44	0.24	0.44	0.41	0.52	0.32	0.57	0.58	0.62	0.35	0.49	0.40 ± 0.05
ATSR	0.34	0.51	0.24	0.38	0.25	0.43	0.42	0.51	0.35	0.57	0.52	0.64	0.26	0.51	0.37 ± 0.05
Precipitation	0.34	0.47	0.18	0.29	0.26	0.34	0.30	0.43	0.28	0.57	0.48	0.64	0.53	0.54	-0.44 ± 0.05
PE	0.20	0.38	0.11	0.25	0.08	0.30	0.15	0.33	0.19	0.42	0.31	0.53	0.38	0.44	0.67 ± 0.13

[a]The Pearson's R^2 coefficient and the amplitude factor (A), calculated as the ratio of the simulated CO_2 standard deviation to the observed CO_2 standard deviation, are shown for each model. The scale factor (λ) was optimized for each model to minimize the cost function across all six latitude bands. All reported errors represent standard deviations.

(Table 2). Since the CO_2 response functions were simulated from flux fields normalized to 1 Pg C yr^{-1} standard deviation, the values of λ can be interpreted as the standard deviation of the optimized carbon fluxes (in units of Pg C yr^{-1}) owing to individual climate drivers over the 15 year period.

Among individual terrestrial ecosystem drivers, the temperature-driven NEE model was positively correlated with the observed CO_2 patterns and explained the largest amount of variance across different latitude bands with an average R^2 of 0.46. After optimization, the temperature-driven NEE fluxes had a standard deviation of 0.80 ± 0.07 Pg C yr^{-1} and the adjusted atmospheric CO_2 response function had a standard deviation that was 61% relative to that of the observations (Table 2).

The CO_2 response function from NEE responding to the Palmer Drought Severity Index (PDSI) had the second most explanatory power with a mean R^2 of 0.42 and an adjusted standard deviation (hereafter termed the amplitude factor) that was 55%. The CO_2 patterns arising from PDSI and precipitation were negatively correlated with the observations, indicating that drought stress increased CO_2 growth and decreased terrestrial carbon storage on interannual time scales. The two fire emissions time series, GFED3 and ATSR, were the third most important class of models, with mean R^2 values of 0.36 and 0.34, respectively, and each with an amplitude factor of 51% of the observations. The optimized GFED3 flux standard deviation of 0.40 ± 0.05 Pg C yr^{-1} was 25% higher than the standard deviation of the original GFED3 emissions time series (0.32 Pg C yr^{-1}) but within expected uncertainties [*van der Werf et al.*, 2010]. Although the precipitation and potential evaporation (PE) CO_2 patterns were qualitatively similar to PDSI (Figures 3d–3f), the mean R^2 was only 0.34 for precipitation and 0.20 for PE, in part due to a likely time delay in NEE responses to precipitation anomalies [*Zeng et al.*, 2013].

To isolate the contribution of tropical fluxes to atmospheric CO_2 variability, we ran an additional GEOS-Chem simulation for each of the drivers described above, considering only fluxes between 23°N and 23°S. The CO_2 variability explained by tropical NEE fluxes had similar Pearson's R^2 coefficients as the global models even in the extratropics (Table 3), confirming earlier work showing that tropical ecosystem responses to climate influence CO_2 variability globally [*Bousquet et al.*, 2000; *Rayner et al.*, 2008]. A key mechanism

Table 3. The Contribution of Terrestrial Ecosystem Fluxes to Interannual Variability in Atmospheric CO_2 From Single-Variable Tropical Flux Models, Similar to Table 2

	Global		60–90°N		23–60°N		0–23°N		0–23°S		23–60°S		60–90°S		
	R^2	A	R^2	A	R^2	A	R^2	A	R^2	A	R^2	A	R^2	A	λ
Temperature	0.48	0.57	0.36	0.39	0.34	0.47	0.51	0.57	0.46	0.65	0.64	0.74	0.57	0.58	0.67 ± 0.06
PDSI	0.38	0.50	0.24	0.32	0.30	0.39	0.37	0.48	0.35	0.59	0.60	0.69	0.42	0.54	-0.48 ± 0.06
GFED3	0.27	0.43	0.05	0.27	0.08	0.33	0.28	0.43	0.32	0.54	0.54	0.59	0.36	0.45	0.34 ± 0.05
ATSR	0.26	0.43	0.10	0.28	0.12	0.34	0.29	0.42	0.33	0.51	0.50	0.57	0.24	0.46	0.33 ± 0.06
Precipitation	0.37	0.49	0.23	0.31	0.28	0.37	0.37	0.46	0.29	0.58	0.52	0.67	0.50	0.53	-0.48 ± 0.06
PE	0.33	0.44	0.21	0.23	0.23	0.27	0.30	0.37	0.28	0.54	0.51	0.69	0.45	0.55	0.79 ± 0.11

Table 4. The Contribution of Terrestrial Ecosystem Fluxes to Interannual Variability in Atmospheric CO_2 From Single-Variable Northern Hemisphere Flux Models, Similar to Table 2

	Global		60–90°N		23–60°N		0–23°N		0–23°S		23–60°S		60–90°S		
	R^2	A	R^2	A	R^2	A	R^2	A	R^2	A	R^2	A	R^2	A	λ
Temperature	0.06	0.00	0.09	0.00	0.02	0.00	0.02	0.00	0.02	0.00	0.11	0.00	0.07	0.00	0.00 ± 0.11
PDSI	0.10	0.24	0.00	0.27	0.01	0.27	0.11	0.27	0.19	0.22	0.26	0.24	0.05	0.19	0.24 ± 0.10
GFED3	0.12	0.26	0.19	0.47	0.23	0.36	0.24	0.26	0.01	0.17	0.01	0.18	0.02	0.14	0.20 ± 0.06
ATSR	0.16	0.34	0.25	0.49	0.25	0.44	0.34	0.32	0.06	0.26	0.04	0.28	0.00	0.22	0.25 ± 0.06
Precipitation	0.20	0.39	0.07	0.49	0.04	0.48	0.27	0.44	0.27	0.31	0.43	0.34	0.15	0.26	0.43 ± 0.10
PE	0.32	0.55	0.05	0.51	0.12	0.57	0.34	0.58	0.42	0.55	0.63	0.60	0.37	0.48	-0.44 ± 0.06

explaining this result is the coupling of large net ecosystem carbon flux anomalies to tropical deep convection that efficiently transports these fluxes poleward in the upper troposphere [*Plumb and Mahlman*, 1987]. With the exception of fire emissions, regression models derived from extratropical Northern Hemisphere fluxes had considerably lower performance metrics than their tropical or global counterparts (Table 4), while extratropical Southern Hemisphere fluxes had almost no impact on CO_2 variability globally (Figure 4). Northern Hemisphere fires explained a much larger fraction of the CO_2 variability at northern middle and high latitudes than tropical or global fires, consistent with past studies documenting considerable interannual variability in boreal forest fires [*Kasischke et al.*, 2005] and the proximity of northern surface stations to these sources.

We developed several regression models combining temperature, drought stress, and fire components. For this analysis, we used PDSI-driven NEE and GFED3 fire emissions since these single-factor regressions performed better than other models within the same class (Table 2), and we focused on fluxes originating in

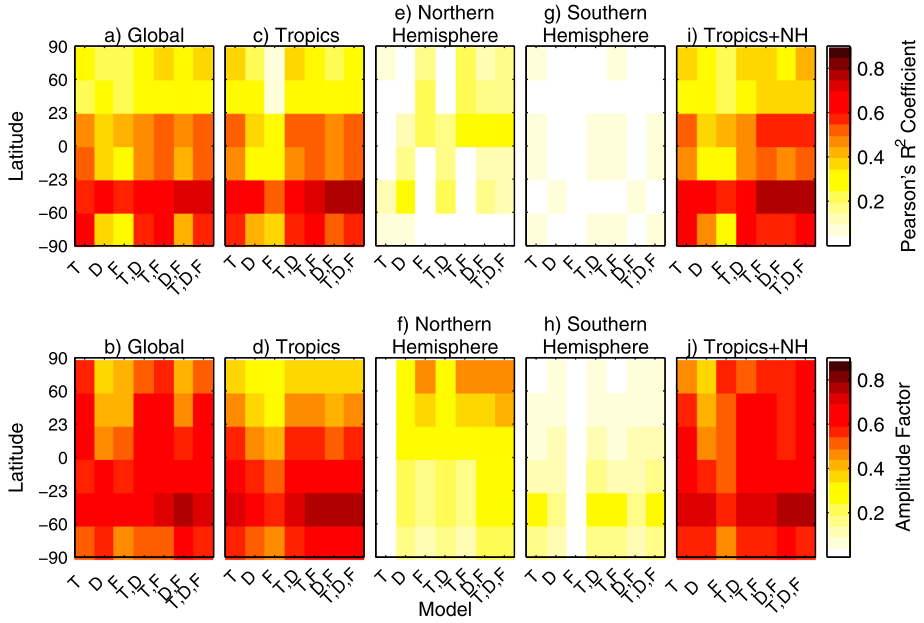

Figure 4. Goodness-of-fit metrics for models of increasing complexity. (top) The Pearson's R^2 coefficient (an indication of correlation between observed and simulated CO_2 variability) and (bottom) the relative amplitude factor (equation (4)) as the goodness-of-fit metric. The value of each metric is shown for (a and b) global fluxes, (c and d) tropical fluxes, (e and f) Northern Hemisphere fluxes, (g and h) Southern Hemisphere fluxes, and (i and j) linear combinations of both tropical and Northern Hemisphere fluxes. For each panel, T represents an NEE model driven solely by temperature, D an NEE model driven solely by PDSI, and F a model driven solely by GFED fire emissions. Other models are a combination of these individual drivers. The relative amplitude is the standard deviation of the simulated CO_2 from the model divided by the standard deviation of observed CO_2 and is an indication of the magnitude of variability contributed by each flux model.

Table 5. Optimal Coefficients (λ) From Each Component in Multidriver Regression Models[a]

Regression Model	Global mean R^2	Tropical T	Tropical PDSI	Tropical GFED	Northern Hemisphere T	Northern Hemisphere PDSI	Northern Hemisphere GFED
Tropical T	0.48	0.67 ± 0.06					
Tropical (T, D)	0.49	0.69 ± 0.14	0.02 ± 0.11				
Tropical (T, F)	0.51	0.54 ± 0.07		0.14 ± 0.04			
Tropical (D, F)	0.48		−0.36 ± 0.05	0.22 ± 0.04			
Tropical (T, D, F)	0.52	0.45 ± 0.14	−0.07 ± 0.10	0.15 ± 0.04			
NH (T, D)	0.12				0.10 ± 0.11	0.27 ± 0.11	
NH (T, F)	0.13				0.03 ± 0.09		0.20 ± 0.06
NH (D, F)	0.16					0.18 ± 0.09	0.17 ± 0.07
NH (T, D, F)	0.17				0.10 ± 0.10	0.21 ± 0.10	0.17 ± 0.06
Best case	0.56	0.43 ± 0.12	−0.16 ± 0.10	0.17 ± 0.04	0.06 ± 0.06	−0.17 ± 0.06	0.13 ± 0.04

[a]The best case model includes six driver variables: temperature, PDSI, and GFED3 contributions in both the tropics and NH.

the tropics and Northern Hemisphere. In general, these models were able to explain more of the CO_2 variability in the Southern Hemisphere than in the Northern Hemisphere, in part due to greater high frequency variability in Northern Hemisphere observations (Figures 1 and 4). Given significant correlations among various drivers (e.g., Figure 3), the scale factors (λ) for the multidriver regression models had reduced magnitudes compared to the corresponding single-driver regressions since the signal amplitude was spread across multiple drivers (Table 5).

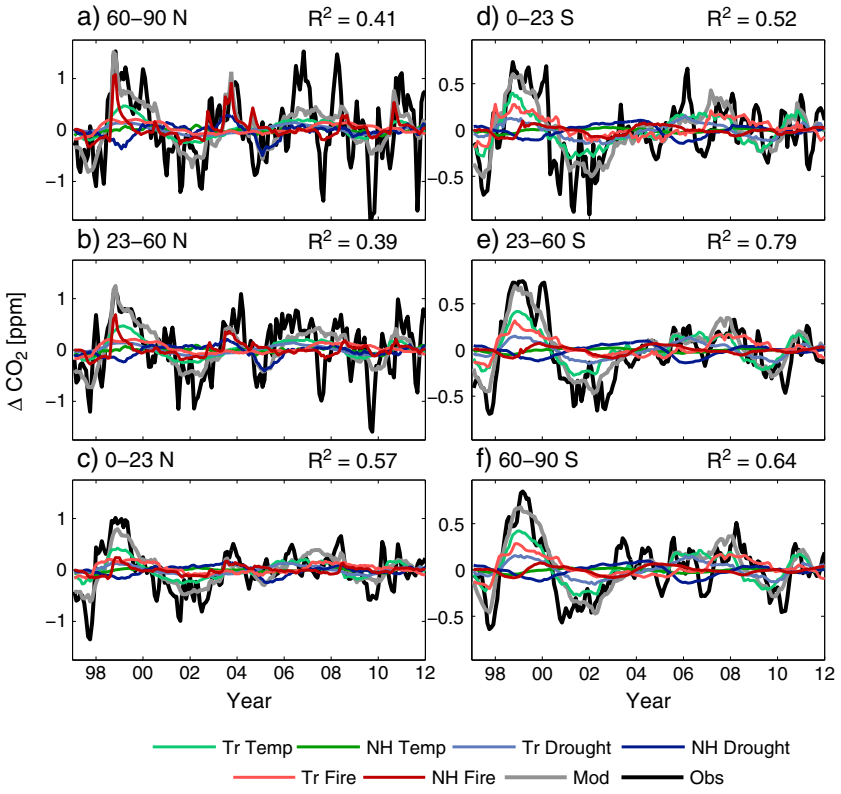

Figure 5. Contributions of tropical (Tr) and Northern Hemisphere (NH) temperature, drought stress (PDSI), and fire emissions (GFED3) to atmospheric CO_2 interannual variability by latitude. The Pearson's R^2 coefficient for each latitude band is given in the upper right hand corner. The best-case model (Mod) is shown with a grey line and the observations (Obs) with a black line. The black lines denoting the observations were not identical to the time series shown in Figure 1 because a refinement to the third-order detrending polynomial was fit based on the residual between the observations and the optimized model. Note also the change in *y* axis scale between the Northern and Southern Hemispheres.

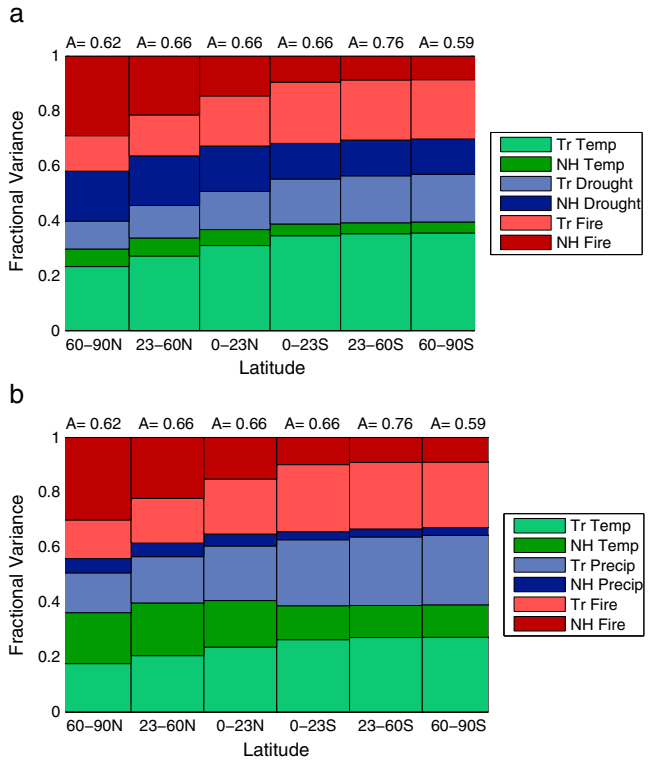

Figure 6. (a) Relative contributions to the simulated variability in atmospheric CO_2 in different latitude bands (*x* axis) from NEE responses to temperature and drought stress (PDSI), and fire emissions (GFED3) originating from the tropics and Northern Hemisphere. The amplitude factor (*A*), calculated as the ratio of the standard deviation of the simulated CO_2 relative to the standard deviation of the observations, is shown for each latitudinal band. (b) Using GPCP precipitation rather than PDSI as a drought stress metric further diminishes the contribution of tropical temperature to interannual variability in atmospheric CO_2.

For a best-case model estimate, we optimized λ coefficients for temperature, drought, and fires from the Northern Hemisphere and tropics simultaneously. This model, comprised of six basis functions, explained 39 to 57% of the observed variability in the Northern Hemisphere and 52 to 79% of the variability in the Southern Hemisphere (Figure 5). The combined contributions from fires and NEE responses to drought stress accounted for 60–70% of the model variability in each latitude belt (Figure 6a). The direct temperature response of NEE contributed between 30–37% of model variability in the Northern Hemisphere and 39–40% in the Southern Hemisphere. Thus, although direct control of NEE by temperature was the single largest driver of observed variability in atmospheric CO_2 (except north of 23°N), the contribution from temperature was smaller than the sum of drought and fire components, contrasting with results reported by [*Wang et al.*, 2013]. We tested an alternative version of the best-case model, substituting precipitation for PDSI as the climate proxy for drought stress, and regression results indicated a further reduction in the contribution from tropical temperature to CO_2 variability (Figure 6b).

Simultaneously accounting for temperature, drought, and fire in the best-case model improved both goodness-of-fit metrics compared to models that assumed only a single driver (Figures 5 and 6, and Table 2). Accounting for correlations among successive monthly observations, the calculated *F* statistic justified the additional degrees of freedom in the best-case model relative to the tropical temperature-only model ($p < 0.01$). Moreover, synthetic data generated from the best-case model, as opposed to those from the tropical temperature-only model, were more consistent with the atmospheric observations (Figure 7). One rationale that has been given for using the present-day temperature sensitivity of the CO_2 growth rate as a constraint on future model projections is that the apparent temperature sensitivity implicitly captures the covarying sensitivity to drought and fire; if that were the case, synthetic CO_2 generated from a tropical temperature-only regression model should yield the same sensitivity to drought and fire as atmospheric observations. However, when the synthetic temperature data were fit serially using single-driver, single-region regression models, the λ values were significantly different from those determined from atmospheric observations, ruling out the possibility that a tropical temperature-only model is sufficient to describe the observations.

Fire contributions to CO_2 variability in the best-case model varied with latitude. Fires had a greater impact in the Northern Hemisphere (33–42%) than in the Southern Hemisphere (30–32%), where fire emissions from boreal forests were large relative to other surface fluxes. In the Northern Hemisphere, the standard deviation of the fire flux in the best-case model increased to 0.13 ± 0.04 Pg C yr^{-1} from the GFED3 baseline of 0.10 Pg C yr^{-1}. In contrast, the standard deviation of the optimized tropical fire emissions was significantly lower than the standard deviation within the tropics from GFED3 (0.17 ± 0.04 Pg C yr^{-1} versus 0.30 Pg C yr^{-1}).

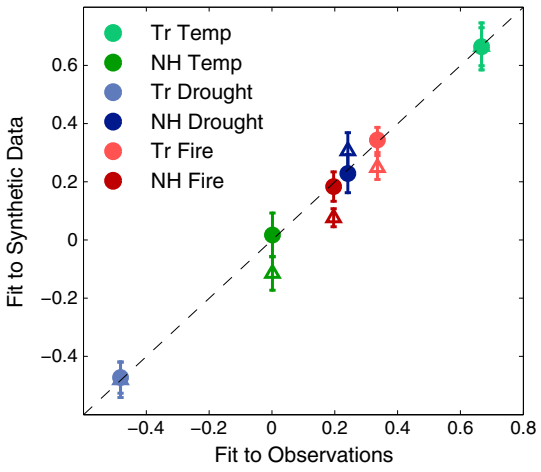

Figure 7. Scale factors for single drivers when fit to observations versus when fit to synthetic data derived from tropical temperature-only and best-case regression models. We generated 1000 realizations of synthetic CO_2 using parameter values drawn from the uncertainty distributions of the tropical temperature-only and the best-case regression models, and fit single-driver temperature, drought, and fire response functions to the synthetic data. The individual λ values fit to the synthetic data derived from the best-case model (circles) were consistent with those fit to the observations, while the Northern Hemisphere λ values and tropical fire λ value fit to the temperature-only synthetic data deviated significantly (triangles), ruling out the possibility that the tropical temperature-only model was consistent with the observations ($p < 10^{-3}$).

The ability to isolate the contributions from temperature, drought, and fire in the meridional distribution of CO_2 was lost when these data were aggregated to a global, area-weighted CO_2 time series. For the best-case model described above, the tropical fire contribution decreased by 60% when fit against a globally averaged CO_2 timeseries rather than against the meridional structure of CO_2 (Table 6). In contrast, the optimal flux magnitude for Northern Hemisphere fire emissions increased several fold (Table 6)—an unrealistic increase given available constraints from CH_4 and CO. When we averaged the global mean CO_2 data to annual time steps, the tropical fire emissions component was further reduced. These exercises demonstrated that aggregating CO_2 data over larger spatial scales and longer time scales may mask contributions from fire emissions observed at higher resolutions.

Estimates of the temperature or drought sensitivity of NEE at large temporal and spatial scales are required for ecosystem model evaluation. Specifically, atmospheric CO_2 responses to regionally coherent climate anomalies provide an opportunity to quantify biome-level responses that integrate across regional variations in species composition, moisture availability, and other important drivers of ecosystem processes that are difficult to represent in global models. This information is complementary to canopy-scale responses derived from eddy covariance observations [e.g., *Schwalm et al.*, 2010]. We determined the large-scale sensitivity of NEE to temperature and drought stress by regressing the land area-weighted monthly NEE fluxes derived from our optimized models against the land area-weighted average of monthly temperature or PDSI anomalies (Figure 8). Accounting for fire emissions considerably reduced the sensitivity of NEE to temperature and drought stress inferred from the atmospheric CO_2 observations (Table 7). We found that the temperature sensitivity of tropical NEE was 3.9 ± 0.4 Pg C yr^{-1} K^{-1} when no other climate drivers or fire fluxes were taken into consideration. When we applied the λ value from a model that included global fire emissions, the temperature sensitivity of tropical NEE decreased by 25% to 2.9 ± 0.4 Pg C yr^{-1} K^{-1}. The sensitivity of tropical NEE to temperature was further

Table 6. Optimal Scale Factors (λ) and Globally Averaged Amplitude Factors (A) for Tropical or Northern Hemisphere GFED Fire Emissions Based on Spatial and Temporal Averaging of Monthly Atmospheric CO_2 Data

	Regional Averaging		Global Averaging		Global, Yearly Averaging	
Model Case	λ_{Fire}	A	λ_{Fire}	A	λ_{Fire}	A
Tropical (T, F)	0.14	0.28	0.06	0.13	0.07	0.14
Tropical (D, F)	0.22	0.42	0.18	0.35	0.18	0.38
Tropical (T, D, F)	0.15	0.29	0.05	0.07	0.03	0.03
Northern (T, F)	0.20	0.90	0.40	0.73	0.69	0.74
Northern (D, F)	0.17	0.53	0.39	0.77	0.64	0.77
Northern (T, D, F)	0.17	0.41	0.35	0.41	0.62	0.42
Bestcase, tropical F	0.17	0.19	0.06	0.06	0.00	0.00

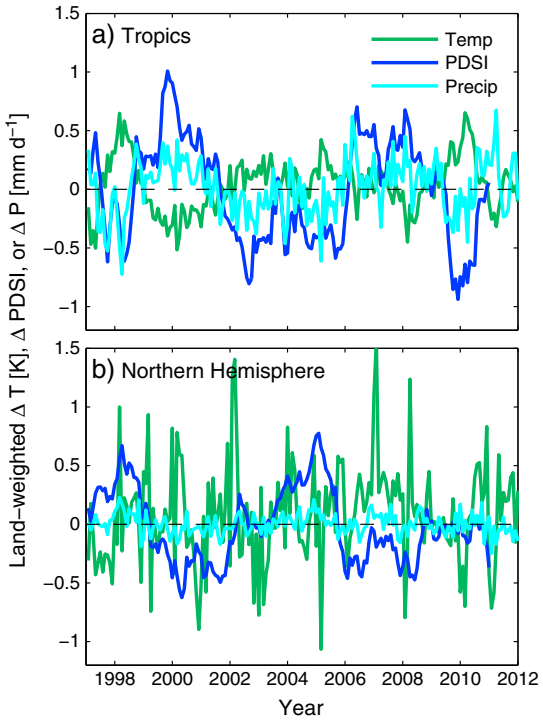

Figure 8. Land-weighted temperature, precipitation, and PDSI anomalies for the tropics and Northern Hemisphere.

reduced to 2.6 ± 0.7 Pg C yr^{-1} K^{-1} when we considered all scale factors from the best-case model (Figure 9). The NEE sensitivity to tropical drought stress likewise decreased by 30%, from -1.1 ± 0.1 Pg C yr^{-1} per unit of PDSI when no other drivers were considered to -0.8 ± 0.1 Pg C yr^{-1} per unit of PDSI when we accounted for global fire emissions (Table 7).

4. Discussion

Our results suggest that the correlation between tropical temperature and the CO_2 growth rate is caused by an assortment of covarying processes, including NEE responses to temperature and drought stress as well as fire emissions in tropical and boreal forest ecosystems. We found that the combined influence of the response of NEE to drought and fire emissions accounted for more of the variability than direct temperature responses of NEE when these drivers were considered simultaneously. These findings have several implications for studies that use contemporary CO_2 variability to constrain ESMs.

First, fire, temperature, and drought responses within ESMs need to be separately and explicitly considered during model evaluation. *Cox et al.* [2013] developed a novel approach for constraining the long-term sensitivity of tropical carbon stocks to warming (γ) in ESMs using contemporary atmospheric CO_2 and temperature observations. The authors showed that a relationship existed across different models between γ and the interannual CO_2 growth rate sensitivity to temperature. In a second step, Cox et al. used observations from the past several decades to show that many models overestimated the observed CO_2 growth rate sensitivity to temperature and thus had γ values that were likely excessive. Several models, however, were near or within the range of the observations. Since many of the models in the ensemble did not have explicit representation of fire processes, removing fire contributions from the observed CO_2 growth rate may enable a more direct comparison with simulated NEE responses to tropical temperature. Our results suggest that after removing fire contributions, the component of the observed CO_2 growth rate variability attributable to tropical NEE would be reduced by approximately 25% (e.g., Table 7), bringing a different set of models into closer agreement with the observed range. Although a more rigorous evaluation is needed, this preliminary estimate strengthens conclusions by Cox et al. that earlier models may have had unrealistically large (negative) values of γ—at least for the nonfire component of the tropical net

Table 7. Sensitivity of NEE to Temperature and Drought Stress (Normalized to a 1 Unit Increase in the Palmer Drought Severity Index) When NEE Responses Were Considered Alone or in Conjunction With Fire Emissions[a]

Flux	Original	Accounting for Fire	Significance of *F* Test
	NEE Sensitivity to Temperature (*Pg C yr*$^{-1}$ K^{-1})		
Tropical NEE	3.9 ± 0.4	2.9 ± 0.4	$p < 0.01$
Global NEE	3.3 ± 0.3	2.4 ± 0.3	$p < 0.01$
	NEE Sensitivity to Drought (*PDSI*) (*Pg C yr*$^{-1}$ per unit of PDSI)		
Tropical NEE	-1.1 ± 0.1	-0.8 ± 0.1	$p < 0.001$
Global NEE	-1.6 ± 0.2	-1.1 ± 0.2	$p < 0.001$

[a]An *F* test was used to compare model pairs with and without fire.

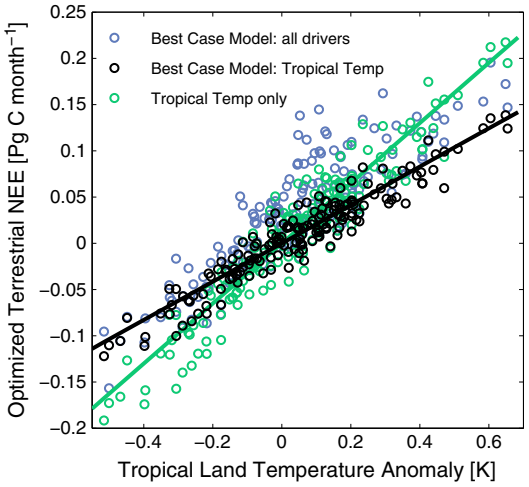

Figure 9. Optimized terrestrial ecosystem flux anomalies for two model cases. The best-case model (blue) represents the sum of fluxes from temperature-driven NEE, PDSI-driven NEE, and fire-driven NEE in the tropics and Northern Hemisphere. Its tropical temperature component has been plotted separately (black). The tropical temperature case (green) only includes temperature-driven fluxes in the tropics.

ecosystem carbon balance. It is important to recognize that while ESM agreement with present-day CO_2 variability and its multiple drivers is necessary to have confidence in climate predictions, it is not sufficient because, on longer time scales, climate changes would be expected to modify processes that are likely of second-order importance to the interannual variations we analyze here, including plant competition and tree mortality.

Second, estimates of the fire contribution to CO_2 variability change significantly with temporal and spatial averaging. The standard deviation of optimized tropical fire emissions decreased by 60–70% when CO_2 variability was averaged globally and by up to 80% when variability was determined from annual, rather than monthly, CO_2 time series. This result underscores the need to consider the full spatial and temporal distribution of atmospheric CO_2 and to use a consistent transport-modeling framework to infer the sensitivities to temperature and drought stress in both models and observations. The extension of column CO_2 time series from GOSAT and forthcoming observations from NASA's Orbiting Carbon Observatory (OCO-2, launched in 2014) may enable future refinements in the partitioning among temperature, drought, and fire contributions to CO_2 variability.

Fire management is one possible lever for reducing CO_2 emissions as the climate warms. In the tropics, where fires are often linked with forest and peatland clearing, different management practices may lead to greater long-term carbon storage. Optimizing long-term development strategies [*Nepstad et al.*, 1999] or more effective use of fire forecasting tools [*Chen et al.*, 2011], for example, may ultimately enable managers to reduce carbon losses. Accurate attribution of interannual variability of CO_2 to fire and NEE responses to drought and temperature also may improve our understanding of drivers of long-term changes in this variability [*Wang et al.*, 2014] and reveal opportunities for decoupling carbon fluxes from drought stress as climate changes.

Analysis of the climate drivers of CO_2 variability at seasonal, interannual, and decadal time scales may ultimately provide a path toward improved climate predictability in ESMs. We stress that capturing variability at these time scales does not ensure accurate climate predictions at longer time scales, but only improves our confidence that important mechanisms are adequately represented. The linkages among temperature, drought, and fire contributions in this study underscore their similar responses to climate variability and the importance of balanced investments in field and modeling research programs that improve our understanding of all of these interactions and their representation in ESMs.

Acknowledgments
This work was supported by the Department of Energy Office of Science Biological and Environmental Research Division, the National Science Foundation Decadal and Regional Climate Prediction using Earth System Models (EaSM) program (NSF AGS 1048890 and AGS 1048827), and NASA Carbon Cycle Science (NASA NNX11AF96G). G.K.A. acknowledges a NOAA Climate and Global Change postdoctoral fellowship. J.B.M. and E.J.D. thank NOAA's Climate Program Office's Atmospheric Chemistry, Carbon Cycle, and Climate (AC4) program for support, including that for collection and analysis of CO_2 observations used in this study. CO_2 observations were downloaded from ftp://aftp.cmdl.noaa.gov/data/trace_gases/co2/flask/surface/. NCEP Reanalysis data were provided by the NOAA/OAR/ESRL PSD, Boulder, Colorado, USA, from their Web site at http://www.esrl.noaa.gov/psd/. CRU temperature data were retrieved from http://www.cru.uea.ac.uk/cru/data/temperature/#datdow. GPCP data were from precip.gsfc.nasa.gov, and GFED data were from http://www.globalfiredata.org/Data/index.html.

References

Adler, R. F., et al. (2003), The Version-2 Global Precipitation Climatology Project (GPCP) monthly precipitation analysis (1979–present), *J. Hydrometeorol.*, *4*(6), 1147–1167, doi:10.1175/1525-7541(2003)004<1147:TVGPCP>2.0.CO;2.

Akagi, S. K., R. J. Yokelson, C. Wiedinmyer, M. J. Alvarado, J. S. Reid, T. Karl, J. D. Crounse, and P. O. Wennberg (2011), Emission factors for open and domestic biomass burning for use in atmospheric models, *Atmos. Chem. Phys.*, *11*(9), 4039–4072, doi:10.5194/acp-11-4039-2011.

Alden, C. B., J. B. Miller, and J. W. C. White (2010), Can bottom-up ocean CO_2 fluxes be reconciled with atmospheric ^{13}C observations?, *Tellus B*, *62*(5), 369–388, doi:10.1111/j.1600-0889.2010.00481.x.

Andreae, M. O., and P. Merlet (2001), Emission of trace gases and aerosols from biomass burning, *Global Biogeochem. Cycles*, *15*(4), 955–966, doi:10.1029/2000GB001382.

Andres, R. J., J. S. Gregg, L. Losey, G. Marland, and T. A. Boden (2011), Monthly, global emissions of carbon dioxide from fossil fuel consumption, *Tellus B*, *63*(3), 309–327, doi:10.1111/j.1600-0889.2011.00530.x.

Arino, O., and J. M. Melinotte (1998), The 1993 Africa fire map, *Int. J. Remote Sens.*, *19*(11), 2019–2023, doi:10.1080/014311698214839.

Atkin, O. (2003), Thermal acclimation and the dynamic response of plant respiration to temperature, *Trends Plant Sci.*, *8*(7), 343–351, doi:10.1016/s1360-1385(03)00136-5.
Bacastow, R. B. (1976), Modulation of atmospheric carbon dioxide by the Southern Oscillation, *Nature*, *261*, 116–118.
Battle, M. O., M. L. Bender, P. P. Tans, J. W. White, J. T. Ellis, T. J. Conway, and R. J. Francey (2000), Global carbon sinks and their variability inferred from atmospheric O_2 and $\delta^{13}C$, *Science*, *287*(287), 2467–2470.
Berry, J., and O. Bjorkman (1980), Photosynthetic response and adaptation to temperature in higher plants, *Annu. Rev. Plant Physiol.*, *31*(1), 491–543, doi:10.1146/annurev.pp.31.060180.002423.
Bonal, D., et al. (2008), Impact of severe dry season on net ecosystem exchange in the neotropical rainforest of French Guiana, *Global Change Biol.*, *14*(8), 1917–1933, doi:10.1111/j.1365-2486.2008.01610.x.
Bousquet, P., P. Peylin, P. Ciais, C. Le Quéré, P. Friedlingstein, and P. P. Tans (2000), Regional changes in carbon dioxide fluxes of land and oceans since 1980, *Science*, *290*(5495), 1342–1346.
Bousquet, P., et al. (2006), Contribution of anthropogenic and natural sources to atmospheric methane variability, *Nature*, *443*(7110), 439–443, doi:10.1038/nature05132.
Bowman, D. M., et al. (2011), The human dimension of fire regimes on Earth, *J. Biogeogr.*, *38*(12), 2223–2236, doi:10.1111/j.1365-2699.2011.02595.x.
Braswell, B. H. (1997), The response of global terrestrial ecosystems to interannual temperature variability, *Science*, *278*(5339), 870–873, doi:10.1126/science.278.5339.870.
Chen, Y., J. T. Randerson, D. C. Morton, R. S. DeFries, G. J. Collatz, P. S. Kasibhatla, L. Giglio, Y. Jin, and M. E. Marlier (2011), Forecasting fire season severity in South America using sea surface temperature anomalies, *Science*, *334*(6057), 787–791, doi:10.1126/science.1209472.
Cox, P. M., D. Pearson, B. B. Booth, P. Friedlingstein, C. Huntingford, C. D. Jones, and C. M. Luke (2013), Sensitivity of tropical carbon to climate change constrained by carbon dioxide variability, *Nature*, *494*(7437), 341–344, doi:10.1038/nature11882.
Dai, A., K. E. Trenberth, and T. T. Qian (2004), A global dataset of Palmer Drought Severity Index for 1870–2002: Relationship with soil moisture and effects of surface warming, *J. Hydrometeorol.*, *5*, 1117–1130.
Davidson, E. A., and I. A. Janssens (2006), Temperature sensitivity of soil carbon decomposition and feedbacks to climate change, *Nature*, *440*(7081), 165–173, doi:10.1038/nature04514.
Dlugokencky, E. J., P. M. Lang, K. Masarie, A. M. Crotwell, and M. J. Crotwell (2013), Atmospheric carbon dioxide dry air mole fractions from the NOAA ESRL carbon cycle cooperative global air sampling network, 1968–2012.
Doney, S. C., I. Lima, R. A. Feely, D. M. Glover, K. Lindsay, N. Mahowald, J. K. Moore, and R. Wanninkhof (2009), Mechanisms governing interannual variability in upper-ocean inorganic carbon system and air–sea CO_2 fluxes: Physical climate and atmospheric dust, *Deep Sea Res., Part II*, *56*(8–10), 640–655, doi:10.1016/j.dsr2.2008.12.006.
Doughty, C. E., and M. L. Goulden (2008), Are tropical forests near a high temperature threshold?, *J. Geophys. Res.*, *113*, G00B07, doi:10.1029/2007JG000632.
Farquhar, G. D., and M. L. Roderick (2003), Pinatubo, diffuse light, and the carbon cycle, *Science*, *299*(5615), 1997–1998, doi:10.1126/science.1080681.
Francey, R. J., P. P. Tans, C. E. Allison, I. G. Enting, J. W. C. White, and M. Trolier (1995), Changes in oceanic and terrestrial carbon uptake since 1982, *Nature*, *373*(6512), 326–330.
Frölicher, T. L., F. Joos, C. C. Raible, and J. L. Sarmiento (2013), Atmospheric CO_2 response to volcanic eruptions: The role of ENSO, season, and variability, *Global Biogeochem. Cycles*, *27*, 239–251, doi:10.1002/gbc.20028.
Gatti, L. V., et al. (2014), Drought sensitivity of Amazonian carbon balance revealed by atmospheric measurements, *Nature*, *506*(7486), 76–80, doi:10.1038/nature12957.
Gelman, A., X. Li Meng, and H. Stern (1996), Posterior predictive assessment of model fitness via realized discrepancies, *Statistica Sinica*, *6*, 733–807.
Jones, C. D., M. Collins, P. M. Cox, and S. A. Spall (2001), The carbon cycle response to ENSO: A coupled climate–carbon cycle model study, *J. Clim.*, *14*(21), 4113–4129, doi:10.1175/1520-0442(2001)014<4113:TCCRTE>2.0.CO;2.
Jones, P. D., D. H. Lister, T. J. Osborn, C. Harpham, M. Salmon, and C. P. Morice (2012), Hemispheric and large-scale land-surface air temperature variations: An extensive revision and an update to 2010, *J. Geophys. Res.*, *117*, D05127, doi:10.1029/2011JD017139.
Kalnay, E., et al. (1996), The NCEP/NCAR 40-year reanalysis project, *Bull. Am. Meteorol. Soc.*, *77*(3), 437–471, doi:10.1175/1520-0477(1996)077<0437:TNYRP>2.0.CO;2.
Kasischke, E. S., E. J. Hyer, P. C. Novelli, L. P. Bruhwiler, N. H. F. French, A. I. Sukhinin, J. H. Hewson, and B. J. Stocks (2005), Influences of boreal fire emissions on Northern Hemisphere atmospheric carbon and carbon monoxide, *Global Biogeochem. Cycles*, *19*, GB1012, doi:10.1029/2004GB002300.
Keeling, C. D., T. P. Whorf, M. Wahlen, and J. Vanderplicht (1995), Interannual extremes in the rate of rise of atmospheric carbon dioxide since 1980, *Nature*, *375*, 666–670.
Keppel-Aleks, G., et al. (2013), Atmospheric carbon dioxide variability in the Community Earth System Model: Evaluation and transient dynamics during the twentieth and twenty-first centuries, *J. Clim.*, *26*(13), 4447–4475, doi:10.1175/jcli-d-12-00589.1.
Langenfelds, R. L., R. J. Francey, B. C. Pak, L. P. Steele, J. Lloyd, C. M. Trudinger, and C. E. Allison (2002), Interannual growth rate variations of atmospheric CO_2 and its $\delta^{13}C$, H_2, CH_4, and CO between 1992 and 1999 linked to biomass burning, *Global Biogeochem. Cycles*, *16*(3), 1048, doi:10.1029/2001GB001466.
Mahecha, M. D., et al. (2010), Global convergence in the temperature sensitivity of respiration at ecosystem level, *Science*, *329*(5993), 838–840, doi:10.1126/science.1189587.
Nassar, R., et al. (2010), Modeling global atmospheric CO_2 with improved emission inventories and CO_2 production from the oxidation of other carbon species, *Geosci. Model Dev.*, *3*(2), 689–716, doi:10.5194/gmd-3-689-2010.
Nepstad, D. C., et al. (1999), Large-scale impoverishment of Amazonian forests by logging and fire, *Nature*, *398*(6727), 505–508.
Nevison, C. D., N. M. Mahowald, S. C. Doney, I. D. Lima, G. R. van der Werf, J. T. Randerson, D. F. Baker, P. Kasibhatla, and G. A. McKinley (2008), Contribution of ocean, fossil fuel, land biosphere, and biomass burning carbon fluxes to seasonal and interannual variability in atmospheric CO_2, *J. Geophys. Res.*, *113*, G01010, doi:10.1029/2007JG000408.
Nobre, P., and J. Shukla (1996), Variations of sea surface temperature, wind stress, and rainfall over the tropical Atlantic and South America, *J. Clim.*, *9*(10), 2464–2479, doi:10.1175/1520-0442(1996)009<2464:VOSSTW>2.0.CO;2.
Plumb, R. A., and J. D. Mahlman (1987), The zonally averaged transport characteristics of the GFDL general circulation/transport model, *J. Atmos. Sci.*, *44*(2), 298–327, doi:10.1175/1520-0469(1987)044<0298:TZATCO>2.0.CO;2.
Rafelski, L. E., S. C. Piper, and R. F. Keeling (2009), Climate effects on atmospheric carbon dioxide over the last century, *Tellus B*, *61*(5), 718–731, doi:10.1111/j.1600-0889.2009.00439.x.

Randerson, J. T., M. V. Thompson, T. J. Conway, I. Fung, and C. B. Field (1997), The contribution of terrestrial sources and sinks to trends in the seasonal cycle of atmospheric carbon dioxide, *Global Biogeochem. Cycles*, *11*(4), 535–560, doi:10.1029/97GB02268.

Randerson, J. T., G. R. van der Werf, G. J. Collatz, L. Giglio, C. J. Still, P. Kasibhatla, J. B. Miller, J. W. C. White, R. S. DeFries, and E. S. Kasischke (2005), Fire emissions from C3 and C4 vegetation and their influence on interannual variability of atmospheric CO_2 and $\delta^{13}CO_2$, *Global Biogeochem. Cycles*, *19*, GB2019, doi:10.1029/2004GB002366.

Rayner, P. J., R. M. Law, C. E. Allison, R. J. Francey, C. M. Trudinger, and C. Pickett-Heaps (2008), Interannual variability of the global carbon cycle (1992–2005) inferred by inversion of atmospheric CO_2 and $\delta^{13}CO_2$ measurements, *Global Biogeochem. Cycles*, *22*, GB3008, doi:10.1029/2007GB003068.

Reichstein, M., et al. (2013), Climate extremes and the carbon cycle, *Nature*, *500*(7462), 287–295, doi:10.1038/nature12350.

Rienecker, M. M., et al. (2011), MERRA: NASA's modern-era retrospective analysis for research and applications, *J. Clim.*, *24*(14), 3624–3648, doi:10.1175/jcli-d-11-00015.1.

Ropelewski, C. F., and M. S. Halpert (1987), Global and regional scale precipitation patterns associated with the El Niño/Southern Oscillation, *Mon. Weather Rev.*, *115*(8), 1606–1626, doi:10.1175/1520-0493(1987)115<1606:GARSPP>2.0.CO;2.

Saleska, S. R., et al. (2003), Carbon in Amazon forests: Unexpected seasonal fluxes and disturbance-induced losses, *Science*, *302*(5650), 1554–1557, doi:10.1126/science.1091165.

Schwalm, C. R., et al. (2010), Assimilation exceeds respiration sensitivity to drought: A FLUXNET synthesis, *Global Change Biol.*, *16*(2), 657–670, doi:10.1111/j.1365-2486.2009.01991.x.

Schwalm, C. R., C. A. Williams, K. Schaefer, I. Baker, G. J. Collatz, and C. Rödenbeck (2011), Does terrestrial drought explain global CO_2 flux anomalies induced by El Niño?, *Biogeosciences*, *8*(9), 2493–2506, doi:10.5194/bg-8-2493-2011.

Suntharalingam, P., D. J. Jacob, P. I. Palmer, J. A. Logan, R. M. Yantosca, Y. Xiao, and M. J. Evans (2004), Improved quantification of Chinese carbon fluxes using CO_2/CO correlations in Asian outflow, *J. Geophys. Res.*, *109*, D18S18, doi:10.1029/2003JD004362.

Todd-Brown, K. E. O., J. T. Randerson, W. M. Post, F. M. Hoffman, C. Tarnocai, E. A. G. Schuur, and S. D. Allison (2013), Causes of variation in soil carbon simulations from CMIP5 Earth system models and comparison with observations, *Biogeosciences*, *10*(3), 1717–1736, doi:10.5194/bg-10-1717-2013.

van der Werf, G. R., J. T. Randerson, G. J. Collatz, L. Giglio, P. S. Kasibhatla, A. F. Arellano Jr., S. C. Olsen, and E. S. Kasischke (2004), Continental-scale partitioning of fire emissions during the 1997 to 2001 El Nino/La Nina period, *Science*, *303*(5654), 73–76, doi:10.1126/science.1090753.

van der Werf, G. R., J. T. Randerson, L. Giglio, G. J. Collatz, M. Mu, P. S. Kasibhatla, D. C. Morton, R. S. DeFries, Y. Jin, and T. T. van Leeuwen (2010), Global fire emissions and the contribution of deforestation, savanna, forest, agricultural, and peat fires (1997–2009), *Atmos. Chem. Phys.*, *10*(23), 11,707–11,735, doi:10.5194/acp-10-11707-2010.

Wang, W., P. Ciais, R. R. Nemani, J. G. Canadell, S. Piao, S. Sitch, M. A. White, H. Hashimoto, C. Milesi, and R. B. Myneni (2013), Variations in atmospheric CO_2 growth rates coupled with tropical temperature, *Proc. Natl. Acad. Sci. U.S.A.*, *110*(32), 13,061–13,066, doi:10.1073/pnas.1219683110.

Wang, X., et al. (2014), A two-fold increase of carbon cycle sensitivity to tropical temperature variations, *Nature*, *506*(7487), 212–215, doi:10.1038/nature12915.

Zeng, F.-W., G. Collatz, J. Pinzon, and A. Ivanoff (2013), Evaluating and quantifying the climate-driven interannual variability in Global Inventory Modeling and Mapping Studies (GIMMS) Normalized Difference Vegetation Index (NDVI3g) at global scales, *Remote Sens.*, *5*(8), 3918–3950.

Zeng, N., A. Mariotti, and P. Wetzel (2005), Terrestrial mechanisms of interannual CO_2 variability, *Global Biogeochem. Cycles*, *19*, GB1016, doi:10.1029/2004GB002273.